RESEARCH ARTICLE

Clean Water

Energy & Environmental Materials WILEY

Fluorescence Behavior of Water-Soluble Porphyrins Immobilized on LTA Zeolite and Its Chlorogenic Acid Polyphenol Sensing in Coffee Wastewater

João Otávio Donizette Malafatti*, Gabriele Magna*, Francesco Pizzoli, Fabrizio Caroleo, Cadia D'Ottavi, Williane da Silva Freitas, Ailton José Moreira, Elaine Cristina Paris, Luiz Henrique Capparelli Mattoso, Corrado Di Natale, and Roberto Paolesse

Chlorogenic acid (CGA) is one of the most common polyphenols found in many fruits, such as coffee cherries, and is among the most economical commodities worldwide. In coffee production, processing and washing require large amounts of water, making wastewater monitoring essential to prevent environmental impact. This work reports the development of a fluorescence-based hybrid sensor designed for the detection of CGA using water-soluble porphyrins immobilized on hierarchical LTA zeolite. The system is based on 5,10,15,20-tetrakis(N-methyl-4-pyridyl)porphyrin (TMPyP) and its Zn(II)-metallated derivative (ZnTMPyP), synthesized directly on the zeolite surface via ion-exchange processes. The hybrid materials (LTA/TMPyP and Zn-LTA/TMPyP) were fully characterized, confirming the preservation of the zeolite structure and the formation of the metalloporphyrin complex within the intercrystalline void network. Fluorescence measurements in phosphate buffer (pH 7.4) showed that Zn-LTA/TMPyP exhibited the best performance for CGA detection, with a detection limit (LOD) of 0.22 nM. To mitigate potential interference from caffeine and caffeic acid, a novel sensing protocol was implemented using these compounds as a controlled background, maintaining high sensitivity (LOD = 0.64 nmol L^{-1}). When tested in real coffee washing water, the sensor quantified CGA at 2.5 ± 0.7 nmol L^{-1}. The measurement accuracy was validated using a nonlinear standard addition method, yielding a recovery of 96.4%, confirming the sensor's ability to compensate for complex matrix effects. The results show that the Zn-LTA/TMPyP hybrid material is a highly efficient, stable, and selective platform for CGA monitoring, with strong potential for integration into portable devices for environmental and agro-industrial applications.

1. Introduction

Chlorogenic acid (CGA) is an important class of polyphenols present in a wide range of herbs and fruits (such as coffee cherry, grape, and citrus). In coffee, 5-O-caffeoylquinic acid is one of the most abundant isomers in brewed grains, and it is associated with controlling oxidative and inflammatory stress.[1,2] This compound exhibits benefits for human health due to its antibacterial, antihypertensive, and antitumoral effects.[3] At the same time, CGA and polyphenols can be partially transferred to water during the processing of foods and crops, thereby potentially conferring toxicity to wastewater and impacting microbial treatment.[4] Thus, monitoring CGA in washing water from agro-industrial activities is essential to ensure its inoffensiveness to the ecosystem and to human use.

Chlorogenic acid (CGA) is commonly determined by HPLC-based methods, such as HPLC–UV, due to their robustness and accessibility. However, these approaches often face limitations in sensitivity, frequently confined to the μmol L^{-1} range, and reduced selectivity in complex matrices, where co-elution and overlapping absorption spectra may interfere with accurate quantification. For applications requiring trace-level detection, such as environmental water monitoring, standard UV detection is often insufficient. While LC–MS/MS significantly enhances both sensitivity and

Dr. J. O. D. Malafatti, Dr. E. C. Paris, Dr. L. H. C. Mattoso
National Nanotechnology Laboratory for Agriculture (LNNA), Embrapa Instrumentação, 13561-206, São Carlos, Brazil
E-mail: jmalafatti@hotmail.com
Dr. G. Magna, Dr. F. Pizzoli, Dr. F. Caroleo, C. D'Ottavi, Dr. W. da Silvia Freitas, Prof. R. Paolesse
Department of Chemical Science and Technologies, Tor Vergata University of Rome, 00133, Rome, Italy
E-mail: gabriele.magna@uniroma2.it
Dr. A. J. Moreira
Institute of Chemistry, São Paulo State University, 14800-900, Araraquara, Brazil
Prof. C. Di Natale
Department of Electronic Engineering, Tor Vergata University of Rome, 00133, Rome, Italy
Centre for Interdisciplinary Research (CIDR), SRM University-AP, Amaravati, Andhra Pradesh 522502, India
The ORCID identification number(s) for the author(s) of this article can be found under https://doi.org/10.1002/eem2.70461.

DOI: 10.1002/eem2.70461

specificity, the high operational costs and the need for sophisticated laboratory infrastructures restrict its use for rapid or in situ screening. Thus, in addition to these classical analytical separation techniques, CGA can also be detected by electrochemical,[5] colorimetric,[6] ultraviolet–visible,[7] and fluorescence-based[8] sensors. To be employed in practical scenarios, sensors must have high sensitivity and selectivity for a specific target, be low-cost, and be amenable to integration into portable platforms, enabling real-time analysis with facile data interpretation.[9] In this context, fluorescence is an excellent transduction mechanism for developing portable, compact devices with exceptional sensitivity, ultralow detection limits, fast response, and ease of operation.[10]

Among fluorophores, porphyrins have garnered significant interest in chemical sensing due to their significance in nature and a broad range of valuable physicochemical and biological properties, including anion binding, metal ion coordination, electron transfer, and the formation of unique supramolecular assemblies.[11–13] The high flexibility of porphyrin structures enables rational design to drive selectivity toward specific target analytes.[14] Porphyrins in sensing arrays have exhibited significant potential for monitoring a range of chemical compounds of interest in biomedical,[15] food quality,[16] and environmental[17] applications. In particular, porphyrins have attracted attention as fluorescence-based receptors because they can be excited in the UV/blue region and emit a fluorescent signal in the red portion of the visible spectrum. This large Stokes shift allows optical devices to easily separate the fluorescence from the source light using low-cost filters, such as those found in commercial smartphones.

One further challenge with fluorophore molecules is controlling their emission intensity, avoiding self-quenching and subsequent aggregation that may affect their fluorescence signal.[18] Indeed, the strategy of confining fluorophores within a rigid framework to suppress π—π aggregation and enhance emission stability aligns with recent advancements in interface engineering and surface passivation. Indeed, sophisticated encapsulation and shell-resurfacing techniques have been recently shown to drastically improve the luminescence performance and operational durability of nanostructured emitters by mitigating surface defects and non-radiative recombination pathways.[19–21] In this context, hybrid systems based on inorganic materials (such as clays or oxides) are good candidates for incorporating porphyrins, offering mutual benefits. While porphyrin macrocycles on the surface of nanostructures can enhance the stability of colloidal suspensions, the immobilization of fluorophores can also enhance their photophysical and chemosensing properties.[22–24] Good candidates for nanostructured scaffolds for porphyrins are zeolites, aluminosilicates with 3D cage structures, which offer elevated chemical stability, surface area, and porosity.[25] Additionally, the presence of counterions within the zeolite structure facilitates ion-exchange and surface modification processes, which, in turn, can enhance the affinity for the target analyte. For example, combinations of these materials in hybrid systems have been reported in the literature to enhance catalysis,[26] fluorescence,[27] and oxidative processes,[28] indicating potential for sensing applications.

Recent papers have reported CGA sensing materials based on carbon dots,[29] metal ions,[30] and complex salts for redox reactions.[31] However, there is still a demand for materials suitable for CGA detection to enhance efficiency and reliability in real-world scenarios. To the best of the authors' knowledge, the use of porphyrins in CGA monitoring has not been reported, especially in hybrid materials such as zeolites. The present work investigates the possibility of using a water-soluble porphyrin, such as TMPyP, supported on LTA zeolite, as a fluorometric indicator for CGA in coffee washing water. TMPyP was specifically selected among water-soluble porphyrins due to its four positively charged N-methylpyridinium meso-substituents, which provide electrostatic complementarity with the negatively charged aluminosilicate surface of LTA zeolite, facilitating strong and homogeneous adsorption without covalent functionalization. Additionally, this article introduces a novel procedure in which exchanging the LTA surface with zinc ions leads to the in situ formation of the corresponding zinc metalloporphyrin during functionalization.

Beyond its analytical performance, the proposed approach stands out for its practical and economic advantages. The synthesis and functionalization procedures are relatively straightforward, requiring no sophisticated equipment and making the sensor accessible for large-scale production. The material cost-per-test is estimated at only a few cents, and compatibility with portable optical readout positions the system as a highly competitive tool for routine CGA monitoring. Ultimately, the study of hybrid sensors combining TMPyP and ZnTMPyP porphyrins on LTA zeolite can advance future sensing platforms for a broader range of chemical compounds.

2. Results and Discussion

2.1. Material Characterization

According to **Figure 1** and procedures reported in the experimental part, LTA was synthesized and functionalized with TMPyP (LTA/TMPyP). Subsequently, LTA was modified with zinc by an ion-exchange procedure. Eventually, the Zn-modified LTA was further functionalized with TMPyP, resulting in the Zn-LTA/TMPyP hybrid material.

Zn^{2+} was selected to provide additional interaction sites between the zeolite framework and the porphyrin receptors. It is well documented that divalent metal ions can coordinate to the nitrogen atoms within the porphyrin core; however, zinc offers distinct advantages over other cations such as Mg^{2+}, Cu^{2+}, or Ni^{2+}. For example, unlike Mg-porphyrins, which are highly prone to demetallation in even mildly acidic or aqueous environments, Zn-porphyrins form more stable adducts. Furthermore, while Cu^{2+} and Ni^{2+} act as strong quenchers of the macrocycle's excited state, zinc metallation preserves fluorescence. Crucially, the zinc metal center in the porphyrin is expected to facilitate axial coordination to functional groups of the target analyte, providing an interaction mechanism that is both stronger and more selective than the hydrogen bonding interactions typical of the free base equivalent.

First, we performed elemental analysis of LTA and Zn-LTA to confirm the successful replacement of Na^+ with Zn^{2+} ions during the ion-exchange process (Figure S1 and Table S1, Supporting Information). The residual Na content of 4.7 wt% (4.5 at%) in the Zn-LTA sample is in good agreement with values reported in the literature[32,33] and reflects intrinsic structural constraints of the LTA framework. Specifically, a fraction of Na^+ ions is located within the β-cages (sodalite cages), which are largely inaccessible to Zn^{2+} ions due to steric hindrance, hydration spheres, and diffusion limitations. Increasing the exchange degree beyond this level would require repeated cycles or more drastic conditions (e.g., higher temperatures or precursor concentrations), which could, however, compromise the crystallinity of the LTA framework. For the hybrid materials (LTA/TMPyP and Zn-LTA/TMPyP), the carbon content (∼15 at%) evidences the presence of

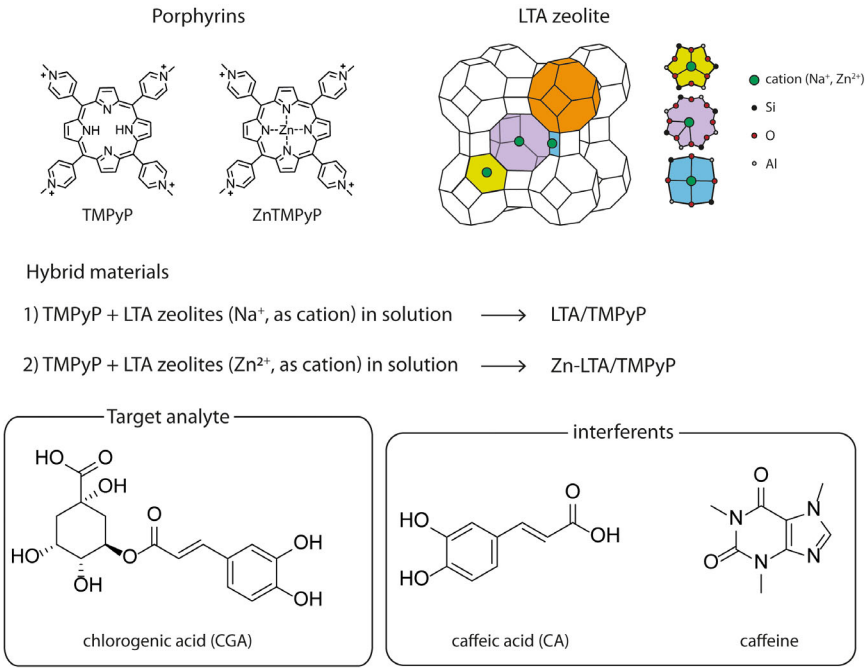

Figure 1. Pristine, hybrid materials, and target analytes utilized in the work.

porphyrin moieties on the zeolite, consistent with the visual evidence of the colored powders.

The structural analysis of LTA zeolite is reported in the X-ray diffractograms (**Figure 2a**). The diffractogram confirms the presence of peaks corresponding to the LTA zeolite and the crystallographic card of the International Centre for Diffraction Data (ICDD) no. 038-0241, indicating the purity of the synthesized phase. Additionally, the hybrid materials of LTA/TMPyP and Zn-LTA/TMPyP confirmed the preservation of the LTA structure upon porphyrin deposition. However, Figure 2a shows that the XRD patterns of Zn-LTA and Zn-LTA/TMPyP exhibit changes in peak intensity when compared with LTA zeolite, non-modified, and LTA/TMPyP hybrid material. Although the characteristic structure of the zeolite was preserved, the reduction in some diffraction peak intensities likely reflects the incorporation of Zn^{2+} ions. This change may be attributed to the presence of Zn^{2+} ions on the external surface of the zeolite, which influences the material's interaction with the X-ray beam. Similar effects have been reported in the literature[34] involving Zn-exchanged zeolites, in which the crystalline framework was preserved despite minimal structural adjustments.

The ATR-FTIR spectra of all zeolite-containing samples display the characteristic features of LTA zeolite (Figure 2b). The broad and intense band in the 1000–1100 cm^{-1} region is assigned to asymmetric Si—O—Al and Si—O—Si stretching vibrations (ν_{as} T—O—T), while contributions at lower wavenumbers are associated with framework vibrations.[35] Compared with LTA, the Zn^{2+}-exchanged zeolite preserves the main FTIR features of the LTA framework, particularly the bands associated with internal T—O—T vibrations and double-ring units, indicating that the zeolitic structure remains preserved after modification. However, changes in band intensity are observed after Zn^{2+} incorporation, especially in the regions around 665 and 545 cm^{-1}, associated with 6MR and 4MR secondary building units respectively,[36] together with the appearance of an additional feature near 893 cm^{-1}, falling within the zeolite transparency window and attributable to the interaction of extra-framework Zn^{2+} cations with the aluminosilicate framework.[37,38] Furthermore, the νas band around 1000 cm^{-1} shows a partial splitting into two resolved components (~980 and ~1100 cm^{-1}), consistent with a symmetry lowering of the local T—O—T environment induced by the stronger electrostatic field of Zn^{2+} relative to Na^{+}, which selectively stiffens the directly coordinated T—O bonds and removes their vibrational degeneracy.[39] Collectively, these results suggest that Zn^{2+} exchange modifies the local vibrational environment of the framework without compromising the overall LTA topology, in agreement with the peak shifts observed in the XRD data (Figure 2a).

Upon TMPyP functionalization, no significant shifts in the main zeolite bands are observed in either LTA/TMPyP or Zn-LTA/TMPyP, indicating that the zeolite framework remains structurally preserved. The absence of detectable porphyrin-specific bands in the functionalized samples is due to the low porphyrin/zeolite molar ratio, which is consistent with a prevalent superficial TMPyP receptor adsorption. This

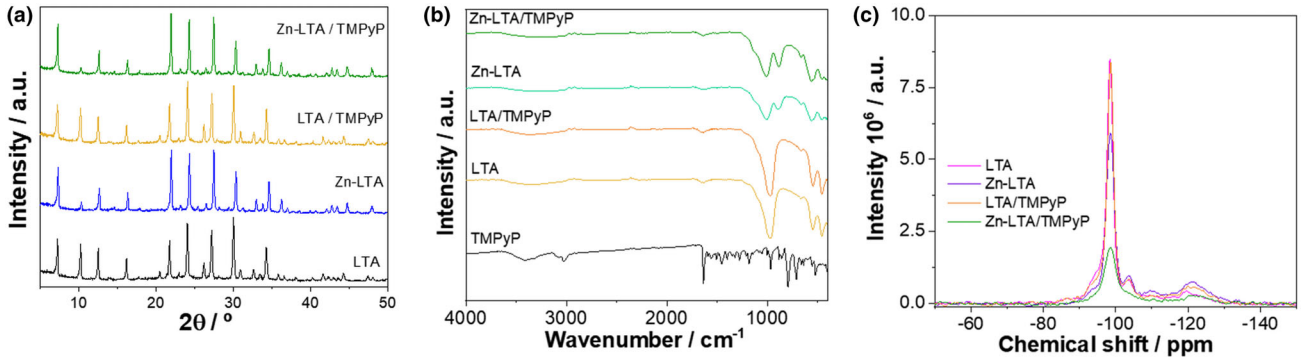

Figure 2. a) XRD structural analysis, b) FTIR, and c) ^{29}Si NMR characterization of LTA, LTA/TMPyP, Zn-LTA, and Zn-LTA/TMPyP.

aspect further explains why the presence of porphyrin does not perturb the aluminosilicate lattice, as indicated by XRD and FTIR characterization.

To evaluate how the coating influences the underlying zeolite, the silicon environments were analyzed by ^{29}Si NMR (Figure 2c). The LTA spectrum shows the expected signals at approximately −98, −104, −109, and −121 ppm, associated with different Si(nAl) sites in the framework. After Zn exchange, the spectra reveal changes in relative intensity and slight peak broadening, indicating modifications in the local electronic environment of silicon. The incorporation of TMPyP results in similar changes, though less noticeable. In contrast, the Zn-LTA/TMPyP sample shows a clear reduction in signal intensity and partial loss of spectral features, suggesting increased local disorder and stronger perturbation of the silicon environment. These observations suggest that the combined presence of Zn and TMPyP enhances interaction with the framework, resulting in a more stable functionalization, while the overall crystalline structure remains unchanged, in agreement with previous results.

The samples were then analyzed morphologically. SEM micrographs (Figure S2a–d, Supporting Information) show that the textural architecture of the synthesized LTA zeolites exhibits a hierarchical organization of Stöber-like monolithic cubes into a more porous, less neatly defined structure. Hierarchical LTA-like structures are well documented in the literature and are prepared via a sol–gel precursor route using TEOS and aluminum isopropoxide; the crystallization kinetics are modulated to favor hierarchical assembly.[40,41]

The micro- and mesoporosity was then assessed by BET characterization (Figure S3, Supporting Information). The nitrogen adsorption–desorption isotherms (77 K) reveal a marked contrast between the sodium forms (LTA: $23.84 \pm 0.66\ m^2\ g^{-1}$, LTA/TMPyP: $18.98 \pm 0.41\ m^2\ g^{-1}$) and the zinc-exchanged forms (Zn-LTA: $282.4 \pm 7.0\ m^2\ g^{-1}$, Zn-LTA/TMPyP: $289.7 \pm 7.5\ m^2\ g^{-1}$), highlighting the critical role of cation-induced pore accessibility. The large discrepancy in BET surface area between (Na)-LTA ($\sim 24\ m^2\ g^{-1}$) and Zn-LTA ($\sim 282\ m^2\ g^{-1}$) is primarily attributed to the "trapdoor effect" and cation-induced pore blockage.[42] In (Na)-LTA, Na^+ cations obstruct the 8-membered ring windows, preventing N_2 molecules from accessing the internal micropores at 77 K. Consequently, the low surface area of the sodium forms (including LTA/TMPyP, $\sim 19\ m^2\ g^{-1}$) represents a consequence of restricted N_2 diffusion through Na^+-blocked 8-ring windows at 77 K, rather than a lack of structural integrity. Conversely, the introduction of divalent Zn^{2+} cations likely clears these apertures, thereby facilitating internal gas diffusion and yielding the markedly higher surface area observed for Zn-LTA, whose isotherm reflects a composite micropore-filling and intercrystalline mesoporous contribution. The relatively low surface area of LTA may also be attributed to the low degassing temperature (200 °C) chosen to ensure the porphyrin's thermal stability. Indeed, the thermogravimetric analysis (TGA) and derivative thermogravimetric (DTG) data indicate a subtle but continuous mass loss not only below but also above 200 °C, particularly for the LTA form, which exhibits an additional minor DTG peak around 300 °C (Figure S4, Supporting Information). The presence of this strongly coordinated hydration water, likely acting in conjunction with the Na^+ cations, appears to contribute to the observed pore inaccessibility under the analytical conditions used (see Data S1, Supporting Information for further details and comments).

It is interesting to note that the morphology of all samples, as previously observed by scanning electron microscopy, aligns with the BET results. The intercrystalline void network of hierarchical LTA is responsible for the secondary mesoporosity reflected in the BET isotherms. Porphyrin incorporation likely occurs at the external crystal surface and within intercrystalline voids, without altering the zeolitic framework, consistent with the TMPyP dimensions ($2 \times 2 \times 0.5\ nm^3$) preclude its entry into the 0.4 nm LTA pore aperture.

Additionally, regarding the BET surface area, LTA/TMPyP shows a decrease compared with LTA, suggesting partial occlusion or reduced pore accessibility due to porphyrin coverage. Conversely, the BET surface area of Zn-LTA/TMPyP ($\sim 290\ m^2\ g^{-1}$) is statistically comparable to that of bare Zn-LTA, confirming that TMPyP incorporation does not compromise the accessible pore structure in this case. This outcome may reflect a different spatial arrangement of the porphyrin macrocycle driven by the coordination interaction between the TMPyP nitrogen atoms and the accessible Zn^{2+} centers at the zeolite surface. Such coordinative anchoring could impose a preferred orientation of the porphyrin plane, modifying the geometry of the intercrystalline space and, consequently, the desorption pathway of N_2, without significantly altering the total probed surface area. Thus, the combined effects of Zn^{2+} exchange, which enhance framework accessibility, and TMPyP incorporation, which modulates the pore environment without blocking gas access, may yield a highly functionalized hierarchical system with preserved, well-defined surface area.

Finally, the zeta potential values remained negative for all samples, ranging from −44 to −51 mV, indicating good colloidal stability (Table S2, Supporting Information).

2.2. Sensing Characterization

Figure 3a,b report the UV–Vis spectra of TMPyP, LTA/TMPyP, and ZnTMPyP, respectively, further confirming the presence of porphyrins in the hybrid materials. In particular, for Zn-LTA/TMPyP, the in situ metalation of TMPyP over LTA mediated by Zn^{2+} ions in the zeolites is evidenced by the changes in the spectral features, such as the red-shift of Soret and Q-bands. For comparison, the spectra of Zn-LTA/TMPyP have been compared with the absorbance profile of metalated TMPyP with Zn in solution (ZnTMPyP, Figure 3b). Furthermore, the porphyrins preserve their fluorescence properties when combined with zeolites (Figure 3c), with the main emission bands localized at 623 nm (Zn-LTA/TMPyP) and 654 nm (LTA/TMPyP). Besides that, the Zn-LTA/TMPyP exhibited a more intense fluorescence emission compared with the free base porphyrin (LTA/TMPyP). This outcome may seem counterintuitive, since the quantum yields of zinc porphyrins are generally lower than those of the free base analogs. However, the higher fluorescence intensity observed for Zn-LTA/TMPyP can be attributed to a more homogeneous distribution of the porphyrin on the zeolite surface, which reduces intermolecular π–π interactions and, consequently, self-aggregation quenching. It is well established that aggregation is one of the primary mechanisms responsible for fluorescence quenching in these macrocycles. This interpretation is further supported by UV–Vis spectroscopy, which shows a better-resolved Soret band for Zn-LTA/TMPyP compared with LTA/TMPyP. **Figure 4** shows the stability of fluorescence emission in aqueous solutions at different pH values. The results indicate that the emission intensity changes slightly for moderate variations around neutral pH. Remarkably, hybrid materials have a more stable fluorescent signal than porphyrins alone. Indeed, the changes in the fluorescence of TMPyP (Figure 4a) and ZnTMPyP (Figure 4c) soluble

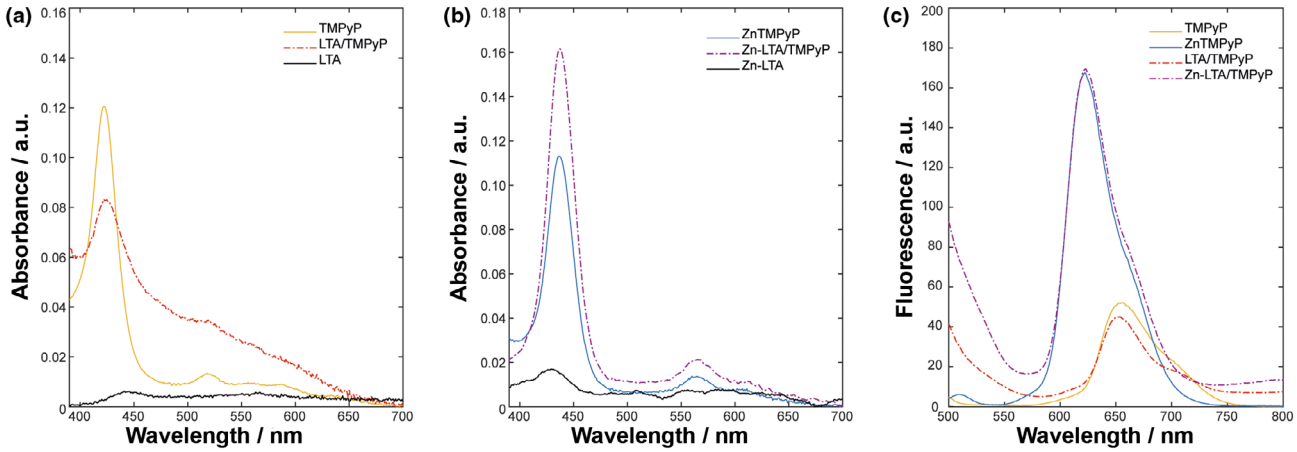

Figure 3. a) UV–Vis absorbance of free base porphyrin, b) Zn-complexes, and c) fluorescence spectra of the sensing materials under PBS buffer. The excitation wavelength for fluorescence was set to the maximum absorption peak.

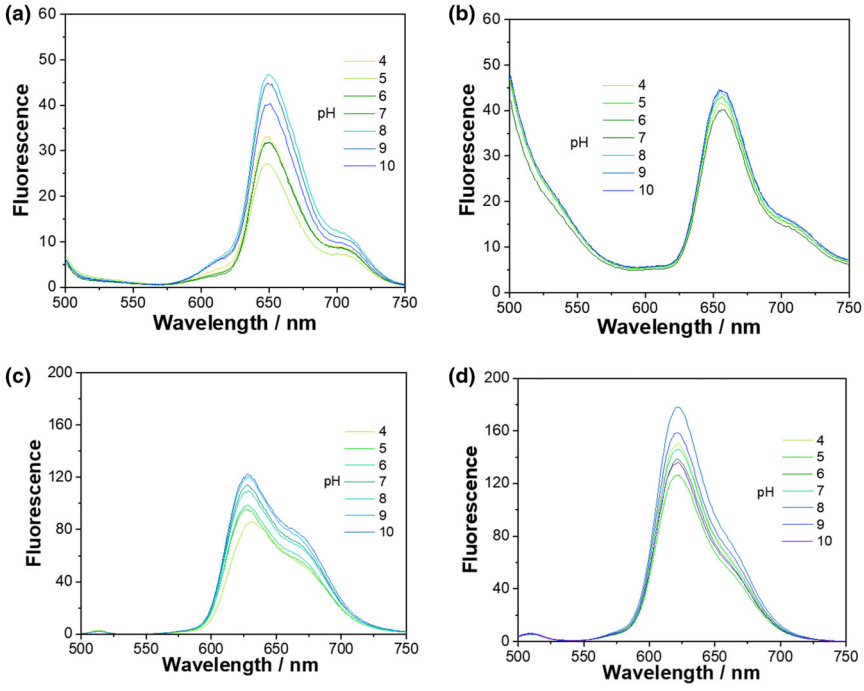

Figure 4. Fluorescence changes in aqueous solution at different pH, considering a) TMPyP, b) LTA/TMPyP, c) ZnTMPyP, and d) Zn-LTA/TMPyP.

porphyrins show changes in both band intensity and maximum peak wavelength. Regarding porphyrins supported on LTA zeolite, LTA/TMPyP (Figure 4b) and Zn-LTA/TMPyP (Figure 4d) are more stable in regions with neutral pH. However, LTA/TMPyP showed higher variation in acid pH and Zn-LTA/TMPyP in the basic medium. One possible hypothesis is that the basic medium favors the formation of $Zn(OH)_2$ species from Zn^{2+} ions leached from Zn-LTA/TMPyP. Thus, pH control using a PBS buffer solution (pH 7.4) is essential for maintaining the stability of sensor characteristics in aqueous solutions to detect polyphenols with acidic properties, such as CGA.

Fluorescence spectra of porphyrins in **Figure 5** show the changes in signal upon the consecutive addition of CGA polyphenol from 1.2 10^{-9} up to 1.2 10^{-3} mol L^{-1}. This figure shows a progressive decrease in emission intensity upon the addition of CGA (from 1.2 $\times 10^{-9}$ to 1.2 $\times 10^{-3}$ mol L^{-1}), consistent with quenching. Possible inner filter effects were excluded according to the criteria detailed in the Experimental Section and Figure S5, Supporting Information.

Figure 6a,b report the changes in fluorescence intensity as the concentration of CGA increases. The normalized fluorescence intensity exhibits a barely linear relationship on a semilogarithmic scale, with a change in slope at high concentrations (approximately 10^{-6} – 10^{-5} mol L^{-1}). All sensors exhibit a behavior characterized by a limited number of binding sites. For pure porphyrins in solution, we employed Hill isotherms to fit the data, obtaining, as expected, a negative cooperative process for both TMPyP and ZnTMPyP (**Figure 6**a,b). The Hill isotherm is defined as:

$$q_e = 1 - \frac{F}{F_0} = \frac{q_{1,max} * {c_e}^h}{k_d + {c_e}^h} \quad (1)$$

where q_e expresses the amount of analyte adsorbed for the c_e concentration of analyte in solution; k_d is the half-saturation constant, and h is the Hill coefficient. In this case, h parameters are less than 1, suggesting negative cooperativity (binding one ligand decreases the affinity for subsequent ligands). Figure 6c,d are characterized by a double Langmuir isotherm, indicating the coexistence of two types of binding sites. The process with the highest binding constant is saturated at low concentration, after which the second interaction mechanism becomes active. Thus, a double sigmoidal trend is clearly visible in these two cases, which can be interpolated by considering a multisite adsorption Langmuir isotherm expressed as:

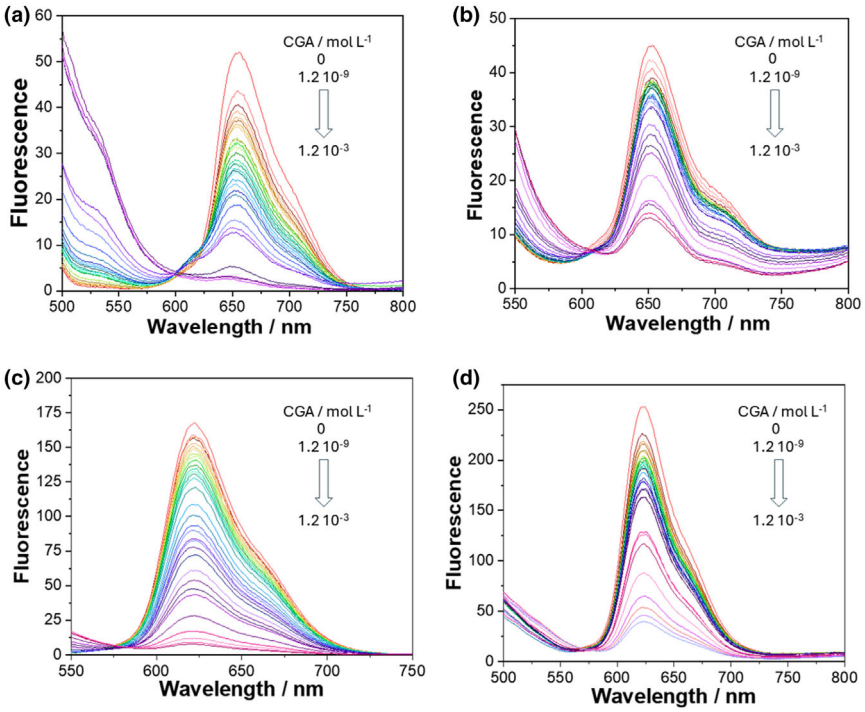

Figure 5. Porphyrin fluorescence spectra against CGA addition (1.2×10^{-9} – 1.2×10^{-3} mol L^{-1}): a) TMPyP, b) LTA/TMPyP, c) ZnTMPyP, and d) Zn-LTA/TMPyP under PBS buffer medium.

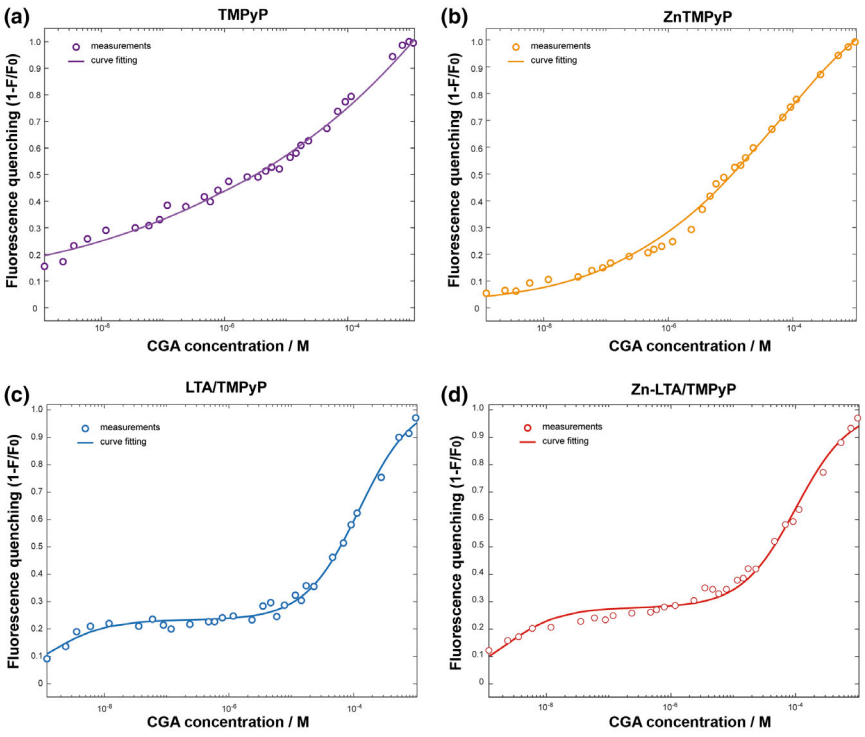

Figure 6. Response curves toward CGA analyte utilizing a) TMPyP, b) ZnTMPyP, c) LTA/TMPyP, and d) Zn-LTA/TMPyP under PBS buffer medium.

$$q_e = 1 - \frac{F}{F_0} = \frac{q_{1,max} * b_1 * C_e}{1 + b_1 * C_e} + \frac{q_{2,max} * b_2 * C_e}{1 + b_2 * C_e} \quad (2)$$

where q_e expresses the amount of analyte adsorbed for the c_e concentration of analyte in solution; $q_{1,max}$ and $q_{2,max}$ parameters express the maximum amount of analyte adsorbed; b_1 and b_2 represent the equilibrium constants for the two distinct interaction mechanisms. Fitting parameters and goodnesses are reported in **Table 1**. In hybrid materials, adsorption is likely due to two distinct mechanisms, each with a distinct equilibrium constant: one for low and one for high concentrations of CGA. This behavior is in agreement with the existence of several potential interaction sites, such as positive charges in the peripheral position of porphyrin and the interaction with the central core of the macrocycle, or by hydrogen bondings, in the case of the free base, or by coordination with Zn metal, in the case of metallated porphyrin.

The calibration curves have been obtained using the normalized fluorescence response on the y-axis as reported in the Experimental section (**Figure 7a–d**), obtaining the values in **Tables 2** and **3**. Regarding LODs, the Zn-LTA/TMPyP sensor exhibited a lower LOD (0.22 nmol L^{-1}), primarily due to its higher reproducibility and stability, resulting in a lower RMSE value.

A comparison across the series reveals that Zn-LTA/TMPyP (Figure 5d) exhibits a significantly more stable fluorescence baseline compared with its non-metallated counterpart (Figure 5b), particularly in the non-emitting regions (500–550 nm and 750–800 nm). This enhanced spectral quality aligns with the previously discussed receptor–zeolite interactions, suggesting that the Zn^{2+} centers promote a more ordered distribution of the porphyrin on the framework while minimizing π—π aggregation between suspended particles. Such a synergistic effect, driven by the immobilization of the porphyrin within the intercrystalline voids, grants higher rigidity to the fluorophore and is consistent with the observation of a more resolved Soret band and reduced light scattering.

Furthermore, the presence of the zinc metal center facilitates axial coordination with the functional groups of CGA. This interaction establishes a more selective and stable bond than the weaker hydrogen bonding typical of the free base analog, thereby reducing the

Table 1. Results for fitting of data in Figure 6 using Equations (1) and (2).

	$q_{1,max}$	k_d ($mol^h\ L^{-h}$)	h	R^2	RMSE
Porphyrins (Hill's isotherm)					
TMPyP	2.015	0.3317	0.1704	0.9855	0.0307
ZnTMPyP	1.3995	0.0386	0.3363	0.9951	0.0213
	$q_{1,max}$	b_1 ($mol^{-1}\ L$)	$q_{2,max}$	b_2 ($mol^{-1}\ L$)	R^2	RMSE
Hybrid materials (Langmuir, multibinding)						
LTA/TMPyP	0.233	7.31E+8	0.805	8.14E+3	0.9946	0.0187
Zn-LTA/TMPyP	0.277	4.67E+8	0.727	1.00E+4	0.9901	0.0249

Table 2. Results for fitting of data in Figure 7 utilizing Langmuir isotherm fitting (Equation (3)).

	Goodness of fit			
	q_{max}	b_1 ($mol^{-1}\ L$)	R^2	RMSE
TMPyP	0.229	6.24E + 8	0.716	0.0444
ZnTMPyP	0.153	5.11E + 8	0.712	0.0290
LTA/TMPyP	0.175	5.10E + 8	0.691	0.0346
Zn-LTA/TMPyP	0.193	5.06E + 8	0.985	0.0064
Zn-LTA/TMPyP[a)]	0.174	3.80E + 8	0.9185	0.0129

[a)]Sensing analysis under background in the presence of CA/CAF (1×10^{-6} mol L^{-1}), vide infra.

influence of nonspecific interactions from the aqueous environment (e.g., solvent molecules or hydroxide ions). Consequently, the fluorescent signal of the Zn-LTA/TMPyP hybrid material remains stable and reproducible across multiple measurements, resulting in reduced data dispersion and overall superior sensing performance.

Additionally, comparing the present work with recent literature reports (**Table 4**), the porphyrin-sensing materials achieved LODs that were lower or comparable to those of carbon dots.[43–46] For these reasons, the Zn-LTA/TMPyP obtained is a potential system for application as a CGA fluorescence sensor. TMPyP supported in Faujasite Y zeolite for detecting antioxidants (reduced glutathione, ascorbic acid, and L-cysteine) has been reported in the literature.[47] The results demonstrated the absence of a new peak in the fluorescence spectra, similar to the present work, indicating that the luminescence quenching mechanism involves electron transfer from the quencher to the porphyrin.

Table 3. Results of sensitivity and limit of detection (LOD) of sensor materials based on porphyrins against CGA polyphenol under PBS buffer medium. Data are calculated using Equations (4) and (5).

Sensor	Sensitivity/10^7 $mol^{-1}\ L$	LOD/nmol L^{-1}
TMPyP	14.29	1.03
ZnTMPyP	7.78	1.23
LTA/TMPyP	8.92	1.28
Zn-LTA/TMPyP	9.75	0.22
Zn-LTA/TMPyP[a)]	6.62	0.64

[a)]Sensing analysis under background in the presence of CA/CAF ($1\ 10^{-6}$ mol L^{-1}), vide infra.

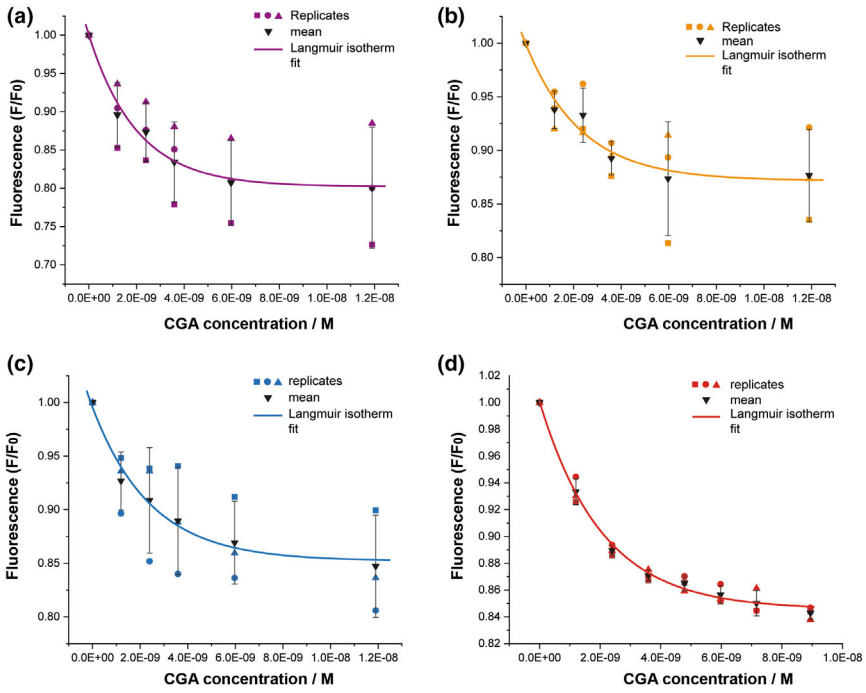

Figure 7. Calibration curves considering lower CGA concentrations in the case of a) TMPyP, b) ZnTMPyP, c) LTA/TMPyP, and d) Zn-LTA/TMPyP under PBS buffer medium. Three replicates have been considered for each concentration.

The sensing behavior of Zn-LTA toward caffeine (CAF) and caffeic acid (CA), a polyphenol derived from CGA, the two main molecules in coffee grains, was investigated to explore the responses to potential interferents. We selected these two components since they are also the most abundant potential interferents in coffee wastewater. **Figure 8**a shows that the addition of both molecules produces a response behavior similar to CGA, predominantly at lower concentrations, with saturation of the response occurring at concentrations above 1 μmol L^{-1}. Cross-sensitivity was further evaluated by using a high concentration of both CA and CAF (1 μmol L^{-1}) as the background. In the presence of a high background concentration of CAF and CA, a small increase in these interferents will not influence the chemosensor response, as we are operating in their saturation region (see the red line in Figure 8a). Remarkably, Figure 8b,c show that the addition of CGA in the presence of a background with CA, CAF, or both CA/CAF maintains almost unaltered the profile of response to CGA, with minor changes in the region of lower concentrations from 1.2×10^{-9} mol L^{-1} to 1.2×10^{-8} mol L^{-1}. Additionally, Figure 8c

Table 4. Comparison of fluorescence sensors and limit of detection (LOD).

CGA fluorescence sensor	Range	LOD	pH buffer	References
Carbon dots	0.15–60 μmol L^{-1}	45 nmol L^{-1}	7	[43]
Molecular imprinted polymer (MIP), based on APTES-TEOS with ZnO quantum dots	0.2–5.3 mg L^{-1}	0.06 mg L^{-1} (0.17 μmol L^{-1})	7	[44]
Carbon dots	10–150 μmol L^{-1}	0.43 μmol L^{-1}	-	[8]
Carbon dots	0.33–2.97 μg L^{-1}	0.12 μg L^{-1} (0.34 nmol L^{-1})	4	[45]
Carbon dots	0.01–1 and 0.1–20 μmol L^{-1}	8.87 nmol L^{-1} and 0.12 μmol L^{-1}	12	[29]
Carbon dots	0.1–220 μmol L^{-1}	0.33 nmol L^{-1}	9	[46]
Zn-LTA/TMPyP	1.2–12 nmol L^{-1}	0.22 nmol L^{-1}	7	This work

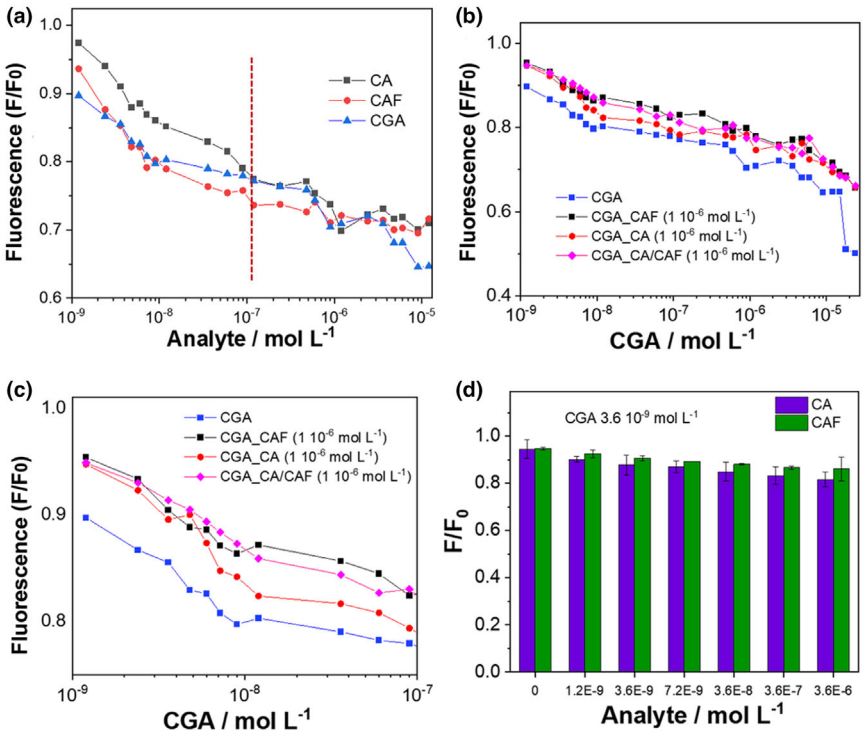

Figure 8. The behavior of Zn-LTA/TMPyP sensor against a) coffee compounds, b) CGA detection in the presence of CA/CAF molecules, c) zoom amplification, and d) interferent addition under the new background.

shows that CAF has a stronger influence on the sensitivity to CGA than CA.

To further validate this approach, a supplementary test was conducted to determine whether the addition of new interferents (CA/CAF) would affect CGA detection. In this case, a set concentration of CGA (3.6×10^{-9} mol L^{-1}) in the presence of the CA/CAF background (1.2×10^{-6} mol L^{-1}) was exposed to the addition of CA/CAF. The results in Figure 8d show that the addition of interferents did not cause significant changes in the Zn-LTA/TMPyP signal, consistent with the measurement error range. A potential protocol for detecting CGA in real samples is illustrated in **Figure 9**a,b. Briefly, the fluorescence at 1 μmol L^{-1} concentration of CA and CAF is considered the reference for F_0 values. Then, the measurements were repeated on the real sample, with 1 μmol L^{-1} concentrations of CA and CAF added to calculate the initial fluorescence intensity, F_0. Finally, the ratio F/F_0 was utilized to estimate the concentration of CGA in samples. The background concentration of CA–CAF prevents the presence of these analytes from influencing the fluorescence.

For this purpose, Figure 9c shows the response curves for the Zn-LTA/TMPyP sensor in the case of the CGA analyte under a 1 μmol L^{-1} background of CA and CAF competitive molecules. Remarkably, the Langmuir-like behavior found here is very close to the one reported in Figure 7d for the pure CGA. Thus, the background correction did not alter the adsorption mechanism in the sensing material. Furthermore, the sensitivity (6.6×10^7 M^{-1}) and LOD (0.64 nM) values reported in Table 3 remained within the expected response range for the Zn-LTA/TMPyP sensor, without background interference.

Figure 9d shows the fluorescence curves (F/F_0) of the sensor in the presence of real samples of water and coffee bean washing water. The fluorescent signal from coffee washing water is lower than that from pure water, indicating the presence of trace amounts of CGA released during washing and demonstrating the sensor's ability to respond to subtle variations in real sample conditions. Furthermore, the coffee washing water exhibited good reproducibility; by applying the external calibration curve (Figure 9c), the CGA concentration was estimated at 2.445 nmol L^{-1}. Despite these preliminary results, an exact analytical quantification of the native concentration was limited by the instrument's quantification limits for traditional methods such as HPLC (see Data S1, Supporting Information). In the absence of an external validation reference, we adopted a self-validation approach to rigorously assess the sensor's performance. This was achieved by comparing the value predicted by the external calibration with the results obtained from a nonlinear standard addition procedure (Figure S6, Supporting Information). This approach evaluates eventual matrix interference and potential signal suppression caused by nontarget species in a real environment. The application of a Langmuir-type fit to the standard addition data yielded a corrected concentration of 2.357 nmol L^{-1}. Compared with the calibration-predicted

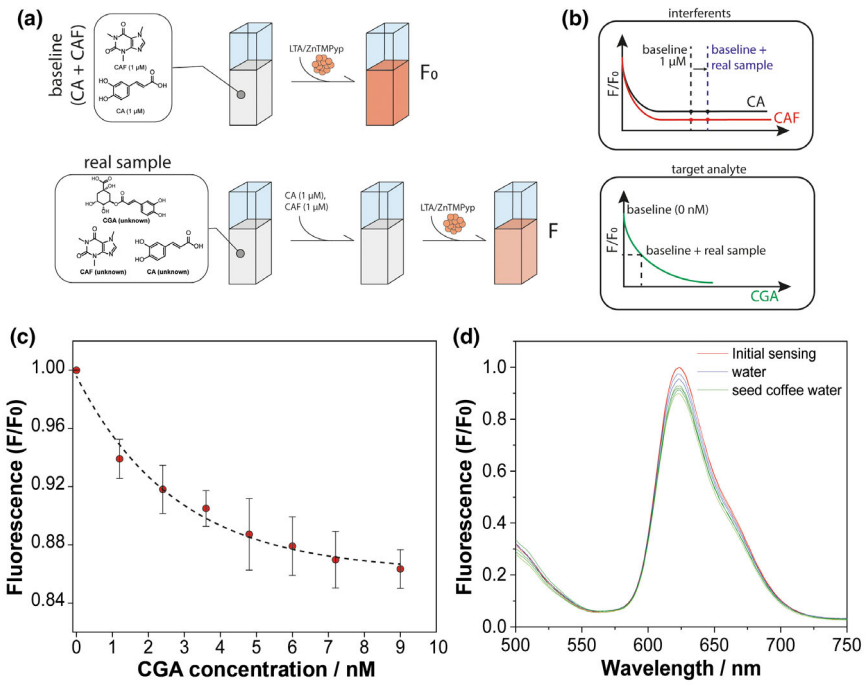

Figure 9. a) Protocol to reduce interfering effects from CA and CAF. b) The preliminary addition of a high concentration of CA and CAF sets the working point in the saturation part of the response curve. c) Zn-LTA/TMPyP calibration curve toward CGA in the presence of a background of CA and CAF. Measurements were performed in triplicate for each concentration. Means and standard deviations have been reported. d) Fluorescence spectra recorder for the real samples of seed coffee washing water under the background (CA/CAF) and PBS buffer medium.

Such a high degree of consistency between the two independent calculation methods (external calibration vs standard addition) provides an objective "self-validation" of the sensor's accuracy in a complex matrix containing multiple unknown interferents, as in real samples. It confirms that the standard addition approach effectively compensates for matrix-specific binding dynamics and ensures high scientific consistency even when traditional benchmarking is unavailable.

As a final consideration, these hybrid materials are primarily intended for disposable (single-use) applications, as they are based on low-cost components (the cost of the hybrid zeolites for a test is estimated to be less than 1 cent). Then, although it is in principle possible to induce CGA desorption to recover and reuse zeolites, this procedure is likely more expensive than using new material. Their practicality is further supported by stability tests, which indicate that both dried powders remain stable for at least 2 months under standard storage conditions (protected from light) and that aqueous suspensions are stable for hours, with no measurable degradation or photobleaching. Finally, the signal normalization procedure adopted for real sample analysis effectively compensates for minor batch-to-batch variations, ensuring consistent analytical performance across different disposable units.

3. Conclusions

In this study, a novel fluorescent hybrid material was developed by anchoring TMPyP porphyrins onto LTA zeolite for the selective sensing of CGA in aqueous media. The ion-exchange modification of LTA with Zn^{2+} ions enabled the in situ formation of the corresponding Zn-metalloporphyrin (ZnTMPyP), enhancing both fluorescence stability and sensitivity. The Zn-LTA/TMPyP composite exhibits excellent fluorescence response for the detection of CGA. As summarized in Table 4, our platform achieves a detection limit of 0.22 nmol L^{-1}, which is highly competitive with, and in many cases superior to, reported values for other fluorescence sensors. These results substantiate the Zn-LTA/TMPyP hybrid as a state-of-the-art platform for trace CGA monitoring in complex environmental and industrial matrices.

The robustness of the hybrid sensor was further validated by its application to real coffee washing water. In the absence of traditional benchmark methods due to trace-level concentrations, a self-validation approach comparing external calibration and nonlinear standard addition confirmed the analytical reliability of the system, yielding a recovery of 96.40%.

These findings substantiate the Zn-LTA/TMPyP hybrid as a state-of-the-art, low-cost, and environmentally friendly platform for monitoring polyphenols in complex matrices. This approach offers a practical solution for controlling wastewater quality in coffee processing and other agro-industrial systems where high sensitivity and matrix resilience are paramount.

4. Experimental Section

Materials: Aluminum isopropoxide ($C_9H_{21}AlO_3$, ≥ 98%), tetraethylorthosilicate (TEOS, ≥ 99%), 5,10,15,20-tetrakis(N-methyl-4-pyridyl)porphyrin (TMPyP, Porphychem 98% min), CGA (CGA, ≥ 95%), sodium chloride (NaCl, ≥ 99.5%), and potassium chloride (KCl, 99%) were purchased from Aldrich-Sigma. Caffeic acid (CA, >98%) and caffeine (CAF, 98%) were purchased from Tokyo Chemical Industry Co. Zinc acetate (Analyticals, 99.5%), sodium phosphate dibasic (Na_2HPO_4, ≥ 98%; Fluka Chemical), and potassium phosphate dibasic (K_2HPO_4, ≥ 99.5%; Merck) were used without further purification.

Zeolite/Porphyrin: LTA zeolite synthesis (LTA)—The synthesis consists of the sol–gel followed by hydrothermal treatment, adapting the methodology described by Meirelles et al.[48] to the stoichiometry $9.5Na_2O{:}Al_2O_3{:}14SiO_2{:}305H_2O$. Initially, the sol–gel was prepared by adding aluminum isopropoxide (7.8 g) to 25 mL of distilled water containing 6.4 g of previously solubilized NaOH. Next, 27.8 g of TEOS was added to the solution and stirred for 1 h at room temperature under magnetic stirring. After 24 h of static aging, the heat treatment was performed at 100 °C for 24 h in a closed stainless steel reactor. The solution containing a white precipitate was water-washed, centrifuged at 2600 g for 10 min (MPW Med. Instruments, M-Universal model), and dried in an oven at 100 °C for 24 h.

LTA zeolite Zn^{2+} modification (Zn-LTA)—The surface modification was achieved by mixing Zn^{2+} ions with LTA zeolite, maintaining a 100 mg M^{2+} g^{-1} zeolite ratio. A Falcon flask containing 10 mL of water was shaken with 100 mg of zeolite and 33.6 mg of previously solubilized zinc acetate for 1 h in an ultrasonic bath. The solutions were centrifuged (2600 g, 10 min at room temperature) and washed five times to remove excess ions. Ultimately, the precipitate was dried in a circulation oven for 24 h at 100 °C.

Zeolite:porphyrin (LTA/TMPyP and Zn-LTA/TMPyP)—The hybrid material based on zeolite and porphyrin was synthesized directly in solution, combining a

previously reported methodology[47] and a 100:1 zeolite-to-porphyrin ratio. 1 mg of TMPyP solubilized in 20 mL of distilled water with 100 mg of LTA or Zn-LTA zeolite, previously dispersed (20 mL water) in an ultrasound bath for 30 min. The solution was homogenized for 1 h in an ultrasonic bath and then centrifuged for 10 min at 1700 g to recover the particulates. The process was repeated 5 times in succession until the solution became transparent. The samples were analyzed using UV–vis and fluorescence spectroscopy to verify the absence of excess porphyrin in the supernatant and to assess their fluorescent properties. The materials were denominated LTA/TMPyP and Zn-LTA/TMPyP, respectively.

ZnTMPyP porphyrin was also synthesized in a classical way as a parameter control to Zn-LTA/TMPyP, adapted from the literature procedure for porphyrin metalation.[49] Sensing materials, analytes, and interferents are schematically depicted in Figure 1.

Characterizations—X-ray diffraction (XRD) was performed using an X-Pert Pro diffractometer, equipped with Cu-Kα radiation ($\lambda = 1.5406$ Å) and a 2θ range of 5–80°, with a scan rate of 1° min^{-1}. The spectroscopic analyses were performed using a UV–vis spectrometer (Cary 60; Agilent) and a fluorometer (RF-1501; Shimadzu). Fourier transform infrared spectroscopy (FTIR) was used to analyze the vibrational modes of the molecular groups and to evaluate possible structural modifications in the materials. The spectra were recorded using a Bruker VERTEX spectrometer with 32 scans over the range 4000–400 cm^{-1} and a resolution of 4 cm^{-1}. Chemical and structural features were further investigated by ^{29}Si solid-state nuclear magnetic resonance (NMR) spectroscopy on a Bruker Avance III HD 400 MHz spectrometer (Billerica, MA, USA) operating at 10 kHz spinning rate. The colloidal properties of the samples were evaluated by zeta potential measurements using a Zetasizer Nano ZS90 (Malvern Instruments, UK). SEM micrographs and elemental analysis have been performed using a scanning electron microscope (SEM) TESCAN VEGA 4 equipped with a GMU chamber and an energy-dispersive X-ray spectrometer (EDS). It is also equipped with a backscattered electron (BSE) detector, and it is able to work in low-vacuum (up to 500 Pa) conditions (with nitrogen or water vapor).

Nitrogen adsorption–desorption isotherms were measured at −196 °C using a Micromeritics Tristar II Plus surface area and pore size analyzer. Before analysis, the samples were degassed overnight at 200 °C under a nitrogen flow. The specific surface area was calculated using the Brunauer–Emmett–Teller (BET) method, over the linear relative pressure range of $p/p_0 = 0.05$–0.15. This range was selected according to the Rouquerol criteria, based on the plot ($V(1 - p/p_0)$ vs p/p_0), where the upper pressure limit is defined by the maximum of the function, ensuring the validity of the BET assumption.[50]

Chlorogenic acid (CGA) sensing assay: Fluorescence studies against the CGA polyphenol were carried out for the sensor based on pure porphyrins (TMPyP and ZnTMPyP) and hybrid materials (LTA/TMPyP and Zn-LTA/TMPyP) in aqueous solution. To minimize primary inner filter effects, the absorbance of the solution at the excitation wavelength was kept below 0.1 (with 1 cm cuvette path length), as recommended by Lakowicz[51] and the IUPAC guidelines.[52] Potential inner filter effects are discussed in the Figure S5, Supporting Information. All the measurements were performed at least in triplicate.

pH stability—The effect of pH was evaluated in the 4–10 range. A solution of NaOH (1 mol L^{-1}) was used to increase the pH from 7 to 10, while a solution of HCl (1 mol L^{-1}) was utilized to decrease the pH from 7 to 4. The analysis was performed by continuously adding NaOH or HCl to a 3 mL aqueous solution. For pure porphyrins, the proper amount of stock solution has been added to achieve an absorbance of around 0.1. For the LTA/TMPyP and Zn-LTA/TMPyP hybrid materials, a 3 mL aqueous suspension at 0.25 mg L^{-1} was used for the measurements.

CGA curve calibration—The CGA spectrophotometric curves were obtained using a plastic cuvette containing 3 mL of a 1:1 mixture of water and phosphate buffer solution (PBS 1×, 10 mM phosphate concentration, pH 7.4). The PBS solution was prepared by mixing NaCl (800 mg), KCl (20 mg), Na_2HPO_4 (144 mg), and KH_2PO_4 (24.5 mg) in 100 mL of distilled water.

CGA stock aqueous solution (7×10^{-3} mol L^{-1}) was used to prepare serial dilutions, obtaining concentrations of 1.2×10^{-3} to 1.2×10^{-9} mol L^{-1}, minimizing sensor concentration variations. The spectra were normalized to account for both dilution factor and initial concentration variations. In this latter case, we considered F/F_0 as the sensor response feature, where F_0 is the initial intensity in the absence of CGA and F is the intensity in the determined CGA concentration.

Limit of detection (LOD)—The limit of detection (LOD) was determined by applying a Langmuir equation fit to fluorescence changes for the CGA samples, ranging in the lower concentrations (from 1.2 to 12 nmol L^{-1})

$$F/F_0 = 1 - \frac{q_{1,\max} * b_1 * C_e}{1 + b_1 * C_e} \quad (3)$$

where C_e is the analyte concentration in solution; $q_{1,\max}$ expresses the maximum amount of analyte adsorbed; b_1 is the equilibrium constant. The LOD value was calculated using Equation (4), obtained through data analysis

$$\text{LOD (mol L}^{-1}) = \frac{3.3 \times \text{RMSE}}{S} \quad (4)$$

where RMSE is the root mean square error resulting from the fitting of F/F_0 versus CGA (mol L^{-1}), and the sensitivity S (mol^{-1} L) is defined as follows:

$$S = \frac{d}{dx}\frac{F}{F_0} \quad (5)$$

calculated around $x = 0$. In the case of Langmuir isotherms, the first derivative at zero is equal to $q_{1,\max}{}^*b_1$ (the equation has been set to obtain positive sensitivities).

Interference molecules and background—The fluorescence response to CAF and CA, compounds found in coffee samples, was evaluated using the same conditions described in the experimental section for the Zn-LTA/TMPyP sensor. The concentrations of CAF and CA ranged from 1.2 10^{-9} to 1.2 $\times 10^{-5}$ mol L^{-1}.

Once CAF and CA molecules were proven to be potential interferents in CGA detection, CAF/CA was added as background to the baseline at a concentration at which the fluorescence signal reached the saturation region. For this purpose, 3 µL of CAF and/or CA from each stock solution (7 mM) was injected in the cuvette, checking if CGA (in the range 1.2×10^{-9} to 2.4×10^{-5} mol L^{-1}) is detectable in the presence of these interferents (1 10^{-6} mol L^{-1}).

The effects of further CAF and CA additions in the new background with an initial concentration of 10^{-6} mol L^{-1} of the CAF/CA were performed by fixing CGA concentration (3.6×10^{-9} mol L^{-1}), inserting from 1.2×10^{-9} to 3.6×10^{-6} mol L^{-1} of these compounds.

Water coffee real sample—The sensor was finally tested using fresh coffee grains (C.A.Vasconcellos LTDA, São Sebastião da Grama, SP, Brazil). Fresh coffee grains (50 g) were washed with 150 mL of distilled water at a 1:3 (v v^{-1}) ratio for 10 min, and the supernatant was separated for analysis. In the case of coffee, the washing water was filtered to remove impurities from the industrial process and then separated for analysis.

Chemical analysis—The CGA analyte in coffee water was verified using a high-performance liquid chromatograph (Agilent 1260 Infinity). Due to the HPLC detection limit and the low CGA concentration, the analyses were performed at 2:1 (v v^{-1}) and 1:1 (v v^{-1}) coffee-to-water ratios. Separation was achieved under isocratic mode, an elution program was applied at a flow rate of 0.8 mL min^{-1} with a mobile phase composed of 90% formic acid (FA, 0.001% v v^{-1})/10% acetonitrile (ACN). The analysis time was 14 min, and the injection volume was 10 µL. Column temperature: 40 °C. Detection using UV–Vis at 210 and 323 nm, and Photoluminescence at $\lambda_{exc.} = 325$ nm and $\lambda_{em.} = 426$ nm was applied. Chromatography column: Poroshell 120 EC-C18, 4.6 × 100 mm, 4 µm.

Acknowledgements

This study was financed by FAPESP (Grant Number 2021/14992-1, 2022/06219-3 and 2023/03632-0). The authors acknowledge Embrapa (Grant Number 11.14.03.001.01.00), FINEP, SisNano, and AgroNano Network for financial support.

The authors are deeply grateful to Prof. Pierluca Galloni and Dr. Alessia Falsetti for their generous availability and the time dedicated to assisting with the experiments and interpreting the data.

Conflict of Interest

The authors declare no conflict of interest.

Supporting Information

Supporting Information is available from the Wiley Online Library or from the author.

Keywords

chlorogenic acid, coffee wastewater, fluorescence sensor, porphyrins, zeolite

Received: January 30, 2026
Revised: May 2, 2026
Published online: May 24, 2026

[1] N. Stefanello, R. M. Spanevello, S. Passamonti, L. Porciúncula, C. D. Bonan, A. A. Olabiyi, J. B. Teixeira da Rocha, C. E. Assmann, V. M. Morsch, M. R. C. Schetinger, *Food Chem. Toxicol.* **2019**, *123*, 298.
[2] N. Liang, D. D. Kitts, *Nutrients* **2016**, *8*, 16.
[3] M. Naveed, V. Hejazi, M. Abbas, A. A. Kamboh, G. J. Khan, M. Shumzaid, F. Ahmad, D. Babazadeh, X. FangFang, F. Modarresi-Ghazani, *Biomed. Pharmacother.* **2018**, *97*, 67.
[4] L. F. Ramos, J. Pluschke, A. M. Bernardes, S. U. Geißen, *Clean. Circ. Bioeconomy* **2023**, *5*, 100048.
[5] R. Chokkareddy, G. G. Redhi, T. Karthick, *Heliyon* **2019**, *5*, e01457.
[6] K. J. Tao, M. D. Castleman, S. Tao, *J. Anal. Test.* **2023**, *7*, 25.
[7] X. Wang, Z. Zeng, Z. Tian, J. Sun, Y. Li, X. Fan, *Food Chem.* **2019**, *278*, 170.
[8] Y. Liu, L. Cao, M. Zan, J. Peng, P. Wang, X. Pang, Y. Zhang, L. Li, W. F. Dong, Q. Mei, *Talanta* **2021**, *233*, 122465.
[9] Y.-H. Shin, M. Teresa Gutierrez-Wing, J.-W. Choi, *J. Electrochem. Soc.* **2021**, *168*, 017502.
[10] H. He, D.-W. Sun, Z. Wu, H. Pu, Q. Wei, *Trends Food Sci. Technol.* **2022**, *119*, 243.
[11] Y. Ding, J. Wang, R. Wang, Y. Xie, *Chin. Chem. Lett.* **2024**, *35*, 109008.
[12] O. Özbek, Ö. Isildak, C. Berkel, *J. Incl. Phenom. Macrocycl. Chem.* **2020**, DOI: 10.1007/s10847-020-01004-y
[13] A. S. Ivanov, A. I. Boldyrev, *Org. Biomol. Chem.* **2014**, *12*, 6145.
[14] D. Monti, S. Nardis, M. Stefanelli, R. Paolesse, C. Di Natale, A. D'Amico, *J Sens* **2009**, *2009*, 856053.
[15] J. Chen, H. Gao, Z. Li, Y. Li, Q. Yuan, *Chin. Chem. Lett.* **2020**, *31*, 1398.
[16] J. Chen, Q. Ma, X. Hu, Y. Gao, X. Yan, D. Qin, X. Lu, *Sens. Actuators B* **2018**, *254*, 475.
[17] Y. Yang, J. Jiang, G. Shen, R. Yu, *Anal. Chim. Acta* **2009**, *636*, 83.
[18] M. Gao, B. Z. Tang, *ACS Sens.* **2017**, *2*, 1382.
[19] Y.-K. Wang, H. Wan, S. Teale, L. Grater, F. Zhao, Z. Zhang, H.-W. Duan, M. Imran, S.-D. Wang, S. Hoogland, L.-S. Liao, *Nature* **2024**, *629*, 586.
[20] Y. Dong, Y.-K. Wang, F. Yuan, A. Johnston, Y. Liu, D. Ma, M.-J. Choi, B. Chen, M. Chekini, S.-W. Baek, L. K. Sagar, J. Fan, Y. Hou, M. Wu, S. Lee, B. Sun, S. Hoogland, R. Quintero-Bermudez, H. Ebe, P. Todorovic, F. Dinic, P. Li, H. T. Kung, M. I. Saidaminov, E. Kumacheva, E. Spiecker, L.-S. Liao, O. Voznyy, Z.-H. Lu, E. H. Sargent, *Nat. Nanotechnol.* **2020**, *15*, 668.
[21] H.-H. Li, Y.-K. Wang, L.-S. Liao, *Adv. Mater.* **2024**, *36*, 2403076.
[22] A. Čeklovski, S. Takagi, *Cent. Eur. J. Chem.* **2013**, *11*, 1132.
[23] J. H. Hassen, J. Silver, *Chem. Biochem. Eng. Q.* **2024**, *38*, 111.
[24] A. Lascu, A. Palade, G. Fagadar-Cosma, I. Creanga, C. Ianasi, I. Sebarchievici, M. Birdeanu, E. Fagadar-Cosma, *Mater. Res. Bull.* **2016**, *74*, 325.
[25] E. C. Paris, J. O. D. Malafatti, H. C. Musetti, A. Manzoli, A. Zenatti, M. T. Escote, *Chem. Eng.* **2020**, *28*, 1884.
[26] R. M. Ion, V. A. Faraon, R. M. Senin, R. C. Fierascu, *Kinet. Mech. Cat* **2016**, *118*, 337.
[27] Y. Tahara, Y. Hirade, K. Arakawa, T. Shimada, T. Ishida, H. Tachibana, S. Takagi, *Molecules* **2024**, *29*, 3738.
[28] T. Tsukamoto, T. Shimada, T. Shiragami, S. Takagi, *Bull. Chem. Soc. Jpn.* **2015**, *88*, 578.
[29] Q. Hu, W. Wang, Z. Quan Yang, L. Xiao, X. Gong, L. Liu, J. Han, *Food Chem.* **2023**, *404*, 134395.
[30] C. V. Popa, A. Vasilescu, S. C. Litescu, C. Albu, A. F. Danet, *Anal. Lett.* **2020**, *53*, 627.
[31] S. Vallejos, D. Moreno, S. Ibeas, A. Muñoz, F. C. García, J. M. García, *Food Control* **2019**, *106*, 106684.
[32] J. I. De León-Ramírez, V. A. Reyes Villegas, S. Pérez-Sicairos, J. R. Chávez Méndez, F. Chávez-Rivas, R. I. Yocupicio-Gaxiola, V. Petranovskii, *PLoS One* **2025**, *20*, e0324997.
[33] J. Yang, J. Cui, H. Zhang, H. Zhang, J. Zhu, *Coatings* **2024**, *14*, 1524.
[34] T. Stanimirova, G. Kirov, *Geol. Balc.* **2023**, *52*, 41.
[35] W. Mozgawa, *J. Mol. Struct.* **2001**, *596*, 129.
[36] M. Król, W. Mozgawa, W. Jastrzębski, K. Barczyk, *Microporous Mesoporous Mater.* **2012**, *156*, 181.
[37] S. Bordiga, C. Lamberti, F. Bonino, A. Travert, F. Thibault-Starzyk, *Chem. Soc. Rev.* **2015**, *44*, 7262.
[38] J. I. D. L. Ramirez, V. A. R. Villegas, R. D. Cadena-Nava, E. Loredo-Garcia, F. Chávez-Rivas, V. González-Torres, V. Petranovskii, *Microporous Mesoporous Mater.* **2024**, *380*, 113295.
[39] A. Koleżyński, A. Mikuła, M. Król, *Spectrosc.* **2016**, *157*, 17.
[40] F. Hasan, R. Singh, G. Li, D. Zhao, P. A. Webley, *J. Colloid Interface Sci.* **2012**, *382*(1), 1.
[41] H. Zhang, Y. Yang, Z. Wang, *J. Membr. Sci.* **2023**, *671*, 121391.
[42] P. Sadeghi, M. B. Myers, V. Pareek, A. Arami-Niya, *Appl. Surf. Sci.* **2024**, *678*, 161037.
[43] H. Yang, L. Yang, Y. Yuan, S. Pan, J. Yang, J. Yan, H. Zhang, Q. Sun, X. Hu, *Spectrochim. Acta A Mol. Biomol. Spectrosc.* **2018**, *189*, 139.
[44] S. Khaksar Haghani, A. A. Ensafi, N. Kazemifard, B. Rezaei, *IEEE Sensors J.* **2020**, *20*, 5691.
[45] Q. Liu, Z. Dong, A. Hao, X. Guo, W. Dong, *Talanta* **2021**, *221*, 121372.
[46] C. J. Pan, D. X. Xin, M. C. Lu, X. Z. Qin, *J. Anal. Chem.* **2023**, *51*, 100334.
[47] S. Wang, H. Zhang, H. Ge, Y. Shi, Z. Li, *Water Sci. Technol.* **2020**, *81*, 121.
[48] M. R. Meirelles, J. O. D. Malafatti, M. T. Escote, A. H. Pinto, E. C. Paris, *Magnetochemistry* **2023**, *9*, 136.
[49] P. Hambright, T. Gore, M. Burton, *Inorg. Chem.* **1976**, *15*, 2314.
[50] J. Rouquerol, P. Llewellyn, F. J. S. S. S. C. Rouquerol, *Stud. Surf. Sci. Catal.* **2007**, *160*, 49.
[51] J. R. Lakowicz, *Principles of Fluorescence Spectroscopy*, 3rd ed., Springer, Boston, MA **2006**.
[52] A. M. Brouwer, *Pure Appl. Chem.* **2011**, *83*, 2213.